Chinese Chemical Letters 33 (2022) 557–561

Contents lists available at ScienceDirect

Chinese Chemical Letters

journal homepage: www.elsevier.com/locate/cclet

Ultrathin Ti_3C_2 nanowires derived from multi-layered bulks for high-performance hydrogen evolution reaction

Weiwei Zhao[a], Beibei Jin[a], Longlu Wang[b], Chengbo Ding[a], Mengyue Jiang[a], Tiantian Chen[a], Shuaihang Bi[a], Shujuan Liu[a], Qiang Zhao[a,b,*]

[a] Key Laboratory for Organic Electronics and Information Displays & Jiangsu Key Laboratory for Biosensors, Institute of Advanced Materials (IAM) Nanjing University of Posts & Telecommunications (NUPT), Nanjing 210023, China
[b] College of Electronic and Optical Engineering & College of Microelectronics, Institute of Flexible Electronics (Future Technology) Nanjing University of Posts & Telecommunications (NUPT), Nanjing 210023 China

ARTICLE INFO

Article history:
Received 14 May 2021
Revised 7 June 2021
Accepted 13 July 2021
Available online 20 July 2021

Keywords:
MXene
Ti_3C_2 nanowires
Ultrathin films
Chemical transformation
Hydrogen evolution reaction

ABSTRACT

One-dimensional ultrathin nanowires (NWs) offer a great deal of promising properties for electrochemical energy storage and conversion due to their nanoscale confinement effect and high surface-to-volume ratios. It is highly desirable to precisely design and synthesize ultrathin Ti_3C_2 NWs in the aspect of size, crystalline structure and composition. Here, we report a simple alkalization strategy to design the ultrathin Ti_3C_2 NWs for hydrogen evolution reaction (HER) by modulating the surface-active sites. The design principle can well improve the amount of the defect sites and ion accessibility to increase the interactions between Ti_3C_2 NWs and H*. The optimized Ti_3C_2 NWs achieve an overpotential of 476 mV at the current density of 10 mA/cm^2 and a Tafel slope of 129 mV/dec for HER catalysis, which are superior to that of Ti_3C_2 nanosheets and m-Ti_3C_2. It paves an avenue for the rational transformation of MXene bulks to one-dimensional NWs catalysts for HER.

With the increasing wastage of fossil fuels and the related environmental pollution, the clean hydrogen (H_2) has attracted much attentions as prospective green and sustainable energy due to its high gravimetric energy density, environmental friendliness and renewability [1,2]. The hydrogen evolution reaction (HER) from water electrolysis has been one of the most desirable strategies for scalable H_2 production, which deeply depends on the high-performance electrocatalysts [3–5]. Inspired by the representative structures, one-dimensional nanowires (1D NWs) enable to realize the wide applications in the field of HER due to their unique characteristics as follows [6,7]: (1) The high surface-to-volume ratios contribute a relatively large active interface between the electrolyte and electrode; (2) The electronic pathways in 1D NWs accelerate the rate of electron transport along the long axis; (3) The confinement effect has a positive impact on the strain relaxation along with volume expansion/contraction while the electrochemical reaction is going on [8,9]. To date, various 1D transition metal compounds nanomaterials such as metal alloys [10], nitrides [11], sulfides [12], selenides [13,14] and phosphides [15,16] have been widely utilized as cut-price and ideal alternatives to the commercial platinum (Pt)-based catalysts. The current studies indicate that the materials with the high conductivity, easy availability, and tunable catalytic sites possess great prospects for the deep exploration of high-efficiency HER catalysts. For instance, the cubic pyrite-phase CoS_2 nanoparticles have exhibited a surprising overpotential of 145 mV at the current density of 10 mA/cm^2 for HER as a result of intrinsic metallic features and good chemical stability [17]. However, the as-obtained efficiencies are still far less than the universal Pt catalysts. It is highly desirable to develop an assortment of new electrode materials for highly efficient HER catalysts.

MXenes, a family of two-dimensional (2D) transition metal carbides, nitrides and carbonitrides, have been developed as emerging energy materials due to the high hydrophilic surface with abundant functional groups (*e.g.*, -OH, -F, -O), and high electronic conductivity (up to 15000 S/cm) [18]. To date, there are more than twenty kinds of MXenes prepared through the chemical etching operation by the fluoride etchant, they are mainly in the form of 2D ultrathin nanosheets (NSs) and widely applied in the construction of energy storage devices as supercapacitor and battery [19,20]. Based on the dimensional engineering on 2D MXene, 1D MXene NWs with remarkable active sites display the enhanced electrochemical performance for HER [21,22]. For example, Hao *et al.* reported 1D NWs interconnected three-dimensional (3D)

* Corresponding author.
E-mail address: iamqzhao@njupt.edu.cn (Q. Zhao).

https://doi.org/10.1016/j.cclet.2021.07.035
1001-8417/

Nb_2C porous frameworks, which exhibit a relative low overpotential of 322 mV towards HER [23]. Guo *et al*. prepared highly active Ti_3C_2 nanofibers with an average width of 50 nm through the combination of hydrolyzation of Ti_3AlC_2 bulks and a subsequent hydrofluoric acid (HF) etching process [24]. However, the large size of Ti_3AlC_2 bulks prevents the full transformation of inner Ti_3AlC_2 into monodispersed NWs in the alkalization process. Therefore, it is still challenging to fabricate ultrathin and monodispersed 1D NWs *via* a facile and inexpensive approach.

Herein, we report a facile alkalization strategy to design Ti_3C_2 NWs with ample active sites for the enhanced HER performance. The scissor role of OH^- can rationally tailor the m-Ti_3C_2 into ultrathin and monodispersed 1D NWs. The design principle can improve the defect sites and ion accessibility to indirectly facilitate the interaction between Ti_3C_2 NWs and H^*. Ti_3C_2 NWs deliver an enhanced HER activity with a low overpotential of 476 mV at the current density of 10 mA/cm^2 and a depressed Tafel slope of 129 mV/dec for HER catalysis, which is lower than that of the Ti_3C_2 NSs and multilayer Ti_3C_2 (m-Ti_3C_2) bulks.

Ti_3AlC_2 powder (99.99 wt% purity) was purchased from 11 Technology Co., Ltd. LiF was purchased from Aladdin. HCl and H_2SO_4 solution (Analytically pure) were purchased from Nanjing Chemical Reagent Co., Ltd. KOH was purchased from Sinopharm Chemical Reagent Co., Ltd. Nafion solution was purchased from Sigma-Aldrich Co., Ltd. SDS was purchased from Shanghai Jingchun Reagent Co., Ltd. SDBS was purchased from Aladdin Chemistry Co., Ltd. PVP (wt 40000) was purchased from Sigma-Aldrich Co., Ltd. CTAB was purchased from Sinopharm Chemical Reagent Co., Ltd. All reagents in this work were used without further purification.

SEM image was characterized by scanning electron microscopy (FE-SEM, Hitachi S-4800). TEM mapping image was measured by transmission electron microscopy (Hitachi HT7700). HRTEM image was operated at an acceleration voltage of 200 kV (FEI Talos F200X). XRD pattern was carried out by X-ray diffractometer (Philips X'pert Pro) with a Cu K_α radiation ($\lambda = 1.5418$ Å). XPS was performed on Thermo ESCALAB 250XI. The electrochemical performance was measured on a CHI660E electrochemical working station (Chenhua, Shanghai, China).

Preparation of m-Ti_3C_2 bulks: Firstly, LiF (0.5 g) was dissolved in HCl (10 mL, 9 mol/L) under stirring for 20 min. Then, the commercial Ti_3AlC_2 bulks (0.5 g) were slowly added in the mixture and heated at 60 °C for 24 h. Afterward, the products were washed with deionized water for five times until the pH surpasses 6. Finally, the samples were dried under vacuum for 12 h.

Preparation of Ti_3C_2 NSs: m-Ti_3C_2 bulks (0.1 g) were dispersed in deionized water (10 mL) and sonicated (60 kHz, 360 W) for 1 h. The dispersion was centrifuged at 3500 rpm for 1 h and collected for the further application.

Preparation of Ti_3C_2 NWs: First, m-Ti_3C_2 bulks (0.08 g) were dispersed in KOH aqueous solution (12 mL, 9 mol/L), and Ar was adopted to remove air for 30 min. Then, the mixture was continuously stirred for 72 h at 35 °C in a sealed state. Next, the products were washed with deionized water and centrifuged at 6000 rpm/min for 5 min each time. Finally, the precipitation was dispersed in deionized water (20 mL) and sonicated (53 kHz, 150 W) for 10 min. After centrifuged at 1000 rpm for 30 min, the supernatant Ti_3C_2 NWs were collected.

Electrochemical measurements: A polished glassy carbon (GC) electrode was served as working electrode while a carbon rod and a Ag/AgCl electrode filled with saturated KCl solution were used as counter and reference electrode, respectively. The electrode was prepared by mixing 2.5 mg of the active materials (*i.e.*, d-Ti_3C_2, ultrathin Ti_3C_2 NSs and ultrathin Ti_3C_2 NWs) in a solution containing 400 μL deionized water, 100 μL ethanol and 10 μL of Nafion (5 wt%) solution, following by ultrasonication (53 kHz, 150 W) for 20 min. 3 μL of the dispersion was deposited on the surface of a glassy carbon (GC) electrode and dried naturally at room temperature. The LSVs for HER were recorded at a sweep rate of 5 mV/s without passing inert gas exhaust. LSV is automatically corrected with 90% iR-compensation.

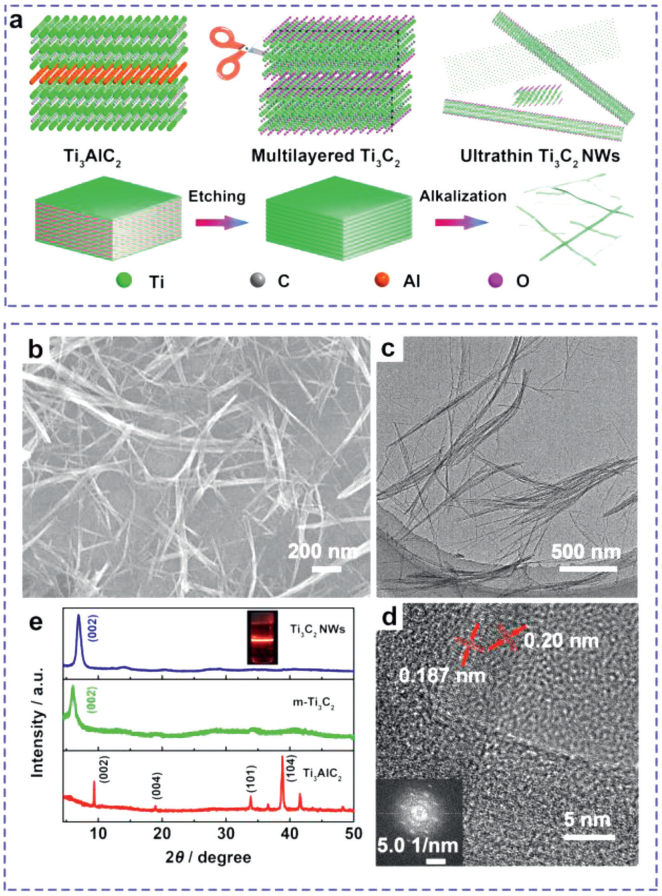

Fig. 1. (a) Schematic diagram of the preparation of ultrathin Ti_3C_2 NWs. (b) SEM image, (c) TEM image and (d) HRTEM image of Ti_3C_2 NWs. Inset of (d) is the corresponding SAED image. (e) XRD patterns of Ti_3C_2 NWs, m-Ti_3C_2 and Ti_3AlC_2. Inset: Tyndall effect of Ti_3C_2 NWs colloidal solution.

The synthetic procedure for Ti_3C_2 NWs is schematically depicted in Fig. 1a. There is a two-step preparation process including thermo-assisted etching and alkalization. First, m-Ti_3C_2 bulks are typically synthesized *via* one-step HF etching of Al atoms from the ternary layered Ti_3AlC_2 phases (Fig. 1a and Fig. S1 in Supporting information). XRD pattern demonstrates the successful removement of Al atom layers from Ti_3AlC_2 bulks (Fig. 1e). Then, the alkalized Ti_3C_2 NWs can be prepared through the continuous stirring of m-Ti_3C_2 bulks in 9 mol/L KOH solution for 72 h. In this process, the abundant OH^- can rationally tailor the exposed scissor sites of 2D NSs, and thus resulting in the morphology transformation into ultrathin 1D NWs. The morphology and structure of Ti_3C_2 NWs are investigated by scanning electron microscopy (SEM), transmission electron microscopy (TEM) and X-ray photoelectron spectroscopy (XPS). SEM image in Fig. 1b shows that Ti_3C_2 NWs have a length ranging from submicrometer to several micrometers. TEM image in Fig. 1c clearly displays that Ti_3C_2 NWs have a width of 5–10 nm. A high-resolution TEM (HRTEM) image shows a highly crystalline structure and an interlayer spacing of 0.187 and 0.2 nm, demonstrating the successful transformation from m-Ti_3C_2 bulks. The corresponding selected area electron diffraction (SAED) image further demonstrates the high crystallinity (inset of Fig. 1d). All peaks in the XRD pattern of ultrathin Ti_3C_2 NWs agree well with the m-Ti_3C_2 bulks, demonstrating the pure phase (Fig. 1e).

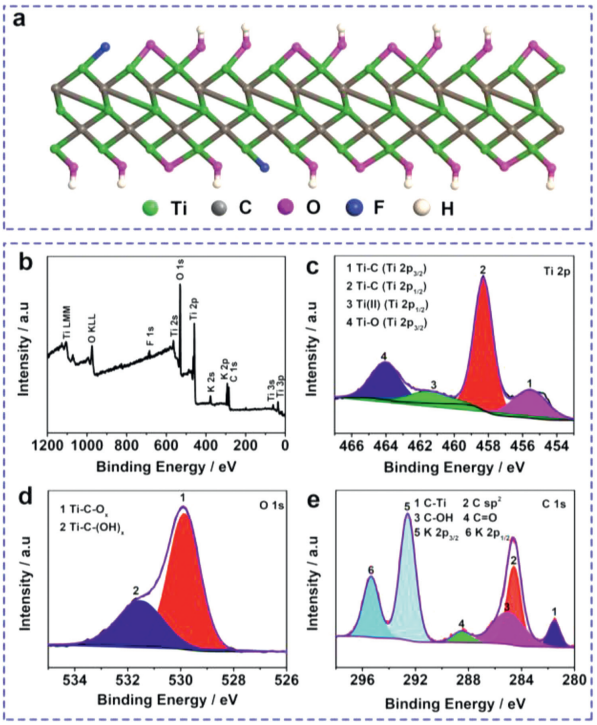

Fig. 2. (a) Structure diagram of Ti_3C_2 NWs. (b) XPS survey spectrum. High-resolution spectra of (c) Ti 2p, (d) O 1s and (e) C 1s.

XPS measurement is carried out to identify the chemical structure of Ti_3C_2 NWs (Fig. 2). It shows that Ti_3C_2 NWs contain the main elements of Ti, C, O, F and K (Fig. 2b). No Al elements are observed in the etched Ti_3C_2 products (Fig. 2b), indicating the full removal of Al layers during the etching process. In the high-resolution Ti 2p spectrum (Fig. 2c), the representative peaks at 455.5 eV, 458.3 eV, 464.1 eV and 461.3 eV are assigned to Ti $2p_{1/2}$ and Ti $2p_{3/2}$ in Ti−C bond, Ti−O bond and Ti(II), respectively, which is in good agreement with the previous literature [25]. Remarkably, the high-resolution O 1s spectrum can be deconvoluted into two peaks at 529.8 eV and 531.5 eV, which are corresponding to the oxygen-containing functional groups (*i.e.*, -O and -OH) existing at the surface of Ti_3C_2 layers (Fig. 2d) [18]. The C 1s for Ti_3C_2 sample is fitted with four doublets cantered at 281.5 eV, 284.5 eV, 285.0 eV and 288.5 eV, which are assigned as C-Ti, C sp^2, C-OH and C=O respectively, (Fig. 2e) [26]. An obvious peak at 295.3 eV and 292.6 eV are assigned to the K $2p_{1/2}$ and K $2p_{3/2}$, ascribing to the anchor of K^+ in the defect sites [27]. The elements detected in XPS spectra well match with the structure diagram, further proving the successful synthesis of Ti_3C_2 NWs.

To get insight into the chemical transformation mechanism of Ti_3C_2 NWs, TEM image is employed to characterize the intermediates collected at 24 h. The epitaxial ultrathin NWs are observed after the alkalization of KOH (Figs. 3a and b) shows the HRTEM images of Ti_3C_2 NSs in the edges of m-Ti_3C_2 bulks. Their lattice fringe spacing of 0.26 nm is corresponding to the (101) interplanar spacing (Fig. 3c) [28]. This result indicates that the crystalline structure of unconverted Ti_3C_2 is well maintained before transforming into NWs. The SAED is consistent with the previous report (Fig. 3d) [29]. The removement of Al layer is important for achieving the ultrathin NWs since the m-Ti_3C_2 precursor generates crevices at the surface of Ti-C sites and subsequently cleaves into ultrathin NWs.

The effects of the amount of m-Ti_3C_2, the kind of surfactants and the concentration of KOH on the alkalization reaction are investigated in control experiments. First, when the amounts of m-Ti_3C_2 bulks increases to 90 mg, they experience an insufficient

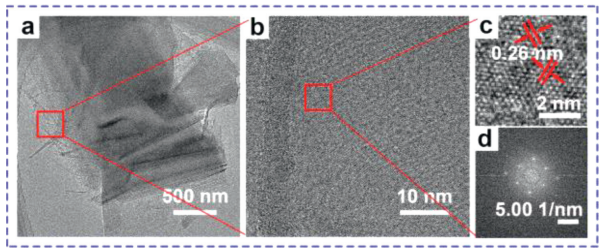

Fig. 3. (a) TEM image, (b,c) HRTEM images and (d) SAED image of Ti_3C_2 intermediate at the reaction time of 24 h.

transformation with residual samples (Fig. S2a in Supporting information). When the amounts of m-Ti_3C_2 bulks decreases to 70 mg, they show a smooth surface and have no obvious transformation into 1D NWs (Fig. S2c in Supporting information). That is because the alkalization process results in the production of the shorter Ti_3C_2 NWs, which are more difficult to separate during centrifugation, resulting in a large proportion of unconverted m-Ti_3C_2 in the final products. Then, the influence of the different surfactants including polyvinyl pyrrolidone (PVP), sodium dodecyl sulfate (SDS), cetyltrimethyl ammonium bromide (CTAB) and sodium dodecyl benzene sulfonate (SDBS) is also investigated (Fig. S3 in Supporting information). As a result, 2D Ti_3C_2 NSs are obtained in all systems. The intercalation of surfactants in the m-Ti_3C_2 is beneficial to the easy peel off of Ti_3C_2 NSs from the m-Ti_3C_2 bulks, whereas it also prevents the exposure of the shearing sites and thus preventing the formation of 1D NWs. Next, the different concentrations of KOH are also explored to treat the m-Ti_3C_2 bulks (Fig. S4 in Supporting information). When KOH concentration increases from 9 mol/L to 10 mol/L, m-Ti_3C_2 bulks are partially converted into Ti_3C_2 NWs (Figs. S4a–d). As the KOH concentration raises to 11 mol/L, a large number of m-Ti_3C_2 bulks still exist (Figs. S4e and f). It is mainly attributed that the excessive KOH will experience the passivation of the cleavable sites. In the control experiment, Ti_3C_2 NSs were fabricated *via* the exfoliation of m-Ti_3C_2, which have a lateral size of 1 μm (Figs. S6a and b in Supporting information). The colloidal solution shows obvious Tyndall effect, and thus proving the good stability (Fig. S6a). The HRTEM image shows that Ti_3C_2 NSs have the lattice spacing of 0.213 nm (Fig. S6c in Supporting information) [30,31], and the corresponding SAED image further demonstrates the high crystallinity (Fig. S6c) [32]. When the ultrathin Ti_3C_2 NSs act as precursors, the ultrathin Ti_3C_2 NWs only form on the surface through the epitaxial transformation (Fig. S5 in supporting information). The presence of KOH makes Ti_3C_2 NSs flocculate into 3D networks, which hinders the further transformation of NWs [33].

The HER activity of the monodispersed Ti_3C_2 NWs is measured using a standard three electrode electrochemical system in 0.5 mol/L H_2SO_4 (Fig. 4). Fig. 4a displays the linear sweep voltammetry (LSV) curves of Ti_3C_2 NWs, Ti_3C_2 NSs and m-Ti_3C_2 for HER at 90% iR correction. Ti_3C_2 NWs deliver a low overpotential of 476 mV at 10 mA/cm^2, which is much lower than that of Ti_3C_2 NSs (543 mV) and m-Ti_3C_2 (659 mV). The enhanced electrochemical performance is resulted from the abundant active sites [24,34]. To further understand the kinetics process, Tafel plots are used to explore the possible steps (Fig. 4b). Ti_3C_2 NWs have a Tafel slope of 129 mV/dec, which is lower than that of the m-Ti_3C_2 bulks (196 mV/dec) and Ti_3C_2 NSs (174 mV/dec), respectively. The fast kinetics of Ti_3C_2 NWs are mainly attributed to the high ion accessibility in 1D structure and low internal contact resistance [35]. Ti_3C_2 NWs manifest a relatively stable and superior performance in acidic electrolyte, which is superior to the previously reported works (Table S1 in Supporting information).

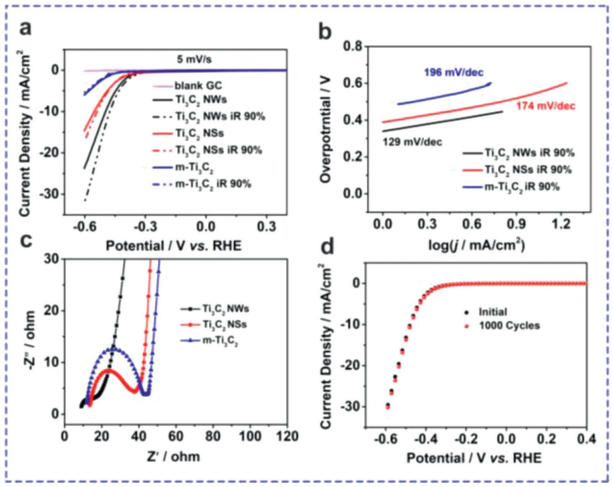

Fig. 4. (a) The LSV curves at initial state (solid line) and at 90% iR correction (dotted line). (b) Tafel plots at 90% iR correction. (c) Nyquist plots of blank GC, Ti_3C_2 NWs, Ti_3C_2 NSs and m-Ti_3C_2. (d) LSV curves of Ti_3C_2 NWs before and after 1000 cycles.

To better understand the interface property and intrinsic activity of Ti_3C_2 NWs and reveal the electron-transfer kinetics in HER, the electrochemical impedance spectroscopy (EIS) is carried out and the Nyquist plots are displayed in Fig. 4c. The semicircle portion at higher frequency is corresponding to the electron transfer-limited process [36]. The semicircle diameter reflects the charge transfer resistance (R_{ct}). It can also be obtained by fitting the impedance spectra to the referencing equivalent circuit. It is found that the R_{ct} of Ti_3C_2 NWs (7.08 Ω) is much lower than that of Ti_3C_2 NSs (11.84 Ω) and m-Ti_3C_2 (31.99 Ω), this is due to the fact that the strongly electronegative fluorine functional group is replaced by a hydroxyl group and the hydrophilicity is enhanced [25,37], suggesting that the NWs can shorten the diffusion pathway for electrons, promote the charge transfer at the interface, and enhance HER performance [38–40]. The Ti_3C_2 NWs also display good cyclic stability before and after 1000 cycles (Fig. 4d). It is mainly ascribed to the synergic effect between unique 1D structure and abundant defect sites. Overall, the mechanism is involved in the following aspects [41,42]: (1) The -OH group terminations can adsorb the H_3O^+ ion and electron to produce an H atom, which experiences the continuous combination for H_2 molecule; (2) The defect sites facilitate the desorption of H^* as well as assist the dissociation of H_2O, making it proceed on a lower potential energy surface.

To further take advantage of 1D NWs, the freestanding Ti_3C_2 NWs film is fabricated through the vacuum-assisted filtration of Ti_3C_2 NWs dispersion on a filter membrane (Fig. 5a). Its integrity can be well maintained after bending at a large angle, demonstrating a good flexibility and foldability (Figs. 5b and c). The cross-sectional SEM image in Fig. 5d indicates that a uniform cross-linking state exists in the freestanding films, showing a thickness of ~3 μm. The surface morphology of the Ti_3C_2 NWs films displays the well-interconnected networks of 1D NWs (Fig. 5e). It is expected to facilitate the rapid ionic/electronic transport and shorten the transport pathways. Cyclic voltammetry (CV) curves of Ti_3C_2 film electrode are measured at a scan rate of 100 mV/s between -0.3 V and 0.4 V (Fig. 5f). After 200 cycles, CV curves are well overlapped. The HER polarization curves in Fig. 5g deliver an overpotential of 528 mV at 10 mA/cm^2, which can be well maintained after 1000 cycles. It is hypothetical that the ions transport can be greatly facilitated by the nanoporous structure in the film due to the shortened ion pathways [43–45]. The freestanding Ti_3C_2 NWs film also shows great potential applications in the fields of photocatalysis [46], electromagnetic interference shielding [47,48], battery [49] and sensor [50,51].

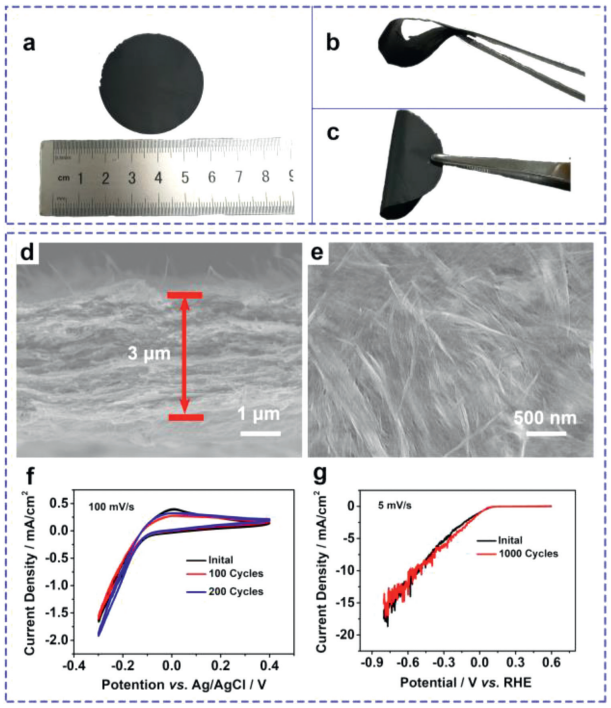

Fig. 5. (a–c) Digital photographs of flexible Ti_3C_2 NWs film. (d) Cross-sectional SEM image and (e) top-view SEM images of Ti_3C_2 NWs film. (f) CV curves of Ti_3C_2 NWs film in 0.5 mol/L H_2SO_4 at a scan rate of 100 mV/s. (g) LSV curves of Ti_3C_2 NWs film in 0.5 mol/L H_2SO_4 at a scan rate of 5 mV/s.

In summary, we have designed ultrathin and monodispersed Ti_3C_2 NWs *via* chemical transformation of m-Ti_3C_2 bulks in KOH solution. The rational tailor of OH^- results in abundant active sites in the ultrathin 1D NWs. In comparison with common Ti_3C_2 NSs, the greatly improved active sites lead to the enhanced HER activity. As a result, the ultrathin Ti_3C_2 NWs deliver a low overpotential of 476 mV at a current density of 10 mA/cm^2, a depressed Tafel slope of 129 mV/dec and low electrochemical resistance. Besides, the Ti_3C_2 NWs show a long-term cycling stability. This synthesis method can further apply to prepare other MXene NWs owing to the large MXene family members, and MXene NWs are promising for applications in batteries, supercapacitors, catalytic and other related fields.

Declaration of competing interest

The authors declare no conflict of interest.

Acknowledgments

This work was supported by the National Natural Science Foundation of China (Nos. 61804082, 21671108 and 51473078), Synergetic Innovation Center for Organic Electronics and Information Displays and Projects of International Cooperation and Exchanges NSFC (Nos. 51811530018), National Natural Science Foundation of China (No. 61935017), the China Postdoctoral Science Foundation Funded Project (No. 2018M642286), National Program for Support of Top-Notch Young Professionals, Scientific and Technological Innovation Teams of Colleges and Universities in Jiangsu Province (No. TJ215006), Priority Academic Program Development of Jiangsu Higher Education Institutions (No. YX03003), Jiangsu Planned Projects for Postdoctoral Research Funds (No. 2019K047A).

Supplementary materials

Supplementary material associated with this article can be found, in the online version, at doi:10.1016/j.cclet.2021.07.035.

References

[1] X. Zhang, Z. Luo, P. Yu, et al., Nat. Catal. 1 (2018) 460–468.
[2] Y. Zhang, L. Xue, C. Liang, et al., Appl. Surface Sci. 561 (2021) 150079.
[3] C. Tan, X. Cao, X. Wu, et al., Chem. Rev. 117 (2017) 6225–6331.
[4] T. Yang, C. Cui, J.Z.H. Rong, et al., Acta Phys. Chim. Sin. 36 (2020) 2003047.
[5] L. Wang, L. Xie, W. Zhao, et al., Chem. Eng. J. 405 (2021) 127028.
[6] G. Zhou, L. Xu, G. Hu, et al., Chem. Rev. 119 (2019) 11042–11109.
[7] Q. Wei, F. Xiong, S. Tan, et al., Adv. Mater. 29 (2017) 1602300.
[8] N. Tapia-Ruiz, A.G. Gordon, C.M. Jewell, et al., Nat. Commun. 11 (2020) 4492.
[9] A.K. Pearce, T.R. Wilks, M.C. Arno, et al., Nat. Rev. Chem. 5 (2021) 21–45.
[10] X. Cao, Y. Han, C. Gao, et al., Nano Energy 9 (2014) 301–308.
[11] C. Wang, W. Qi, Y. Zhou, et al., Chem. Eng. J. 381 (2020) 122611.
[12] P. Zhai, Y. Zhang, Y. Wu, et al., Nat. Commun. 11 (2020) 5462.
[13] W. Feng, W. Pang, Y. Xu, et al., Chem. Electro. Chem. 7 (2020) 31–54.
[14] L. Zhai, T.W. Benedict Lo, Z.L. Xu, et al., ACS Energy Lett. 5 (2020) 2483–2491.
[15] Y. Pei, Y. Cheng, J. Chen, et al., J. Mater. Chem. A 6 (2018) 23220–23243.
[16] S. Xu, H. Zhao, T. Li, et al., J. Mater. Chem. A 8 (2020) 19729–19745.
[17] M.S. Faber, R. Dziedzic, M.A. Lukowski, et al., J. Am. Chem. Soc. 136 (2014) 10053–10061.
[18] W. Zhao, J. Peng, W. Wang, et al., Small 15 (2019) 1901351.
[19] J. Nan, X. Guo, J. Xiao, et al., Small 17 (2021) 1902085.
[20] D. Xiong, X. Li, Z. Bai, et al., Small 14 (2018) 1703419.
[21] P. Lian, Y. Dong, Z.S. Wu, et al., Nano Energy 40 (2017) 1–8.
[22] Y. Dong, S. Zheng, J. Qin, et al., ACS Nano 12 (2018) 2381–2388.
[23] S.Y. Pang, W.F. Io, LW. Wong, et al., Adv. Sci. 7 (2020) 1903680.
[24] W. Yuan, L. Cheng, Y. An, et al., ACS Sustainable Chem. Eng. 6 (2018) 8976–8982.
[25] X. Zhu, B. Liu, H. Hou, et al., Electrochim. Acta 248 (2017) 46–57.
[26] D. Zhang, J. Cao, X. Zhang, et al., ACS Appl. Energy Mater. 3 (2020) 5949–5964.
[27] X. Wang, S. Kajiyama, H. Iinuma, et al., Nat. Commun. 6 (2015) 6544.
[28] J. Tang, T. Mathis, X. Zhong, et al., Adv. Energy Mater. 11 (2021) 2003025.
[29] C. Zhang, B. Anasori, A. Seral-Ascaso, et al., Adv. Mater. 29 (2017) 1702678.
[30] Z. Jin, C. Liu, Z. Liu, et al., Adv. Energy Mater. 10 (2020) 2000797.
[31] R. Qin, M. Hu, X. Li, et al., Nanoscale 12 (2020) 17715–17724.
[32] O. Mashtalir, M. Naguib, V.N. Mochalin, et al., Nat. Commun. 4 (2013) 1716.
[33] D. Zhao, M. Clites, G. Ying, et al., Chem. Commun. 54 (2018) 4533–4536.
[34] N. Li, Y. Jiang, C. Zhou, et al., ACS Appl. Mater. Interfaces 11 (2019) 38116–38125.
[35] B. Zhang, J. Zhu, P. Shi, et al., Ceram. Int. 45 (2019) 8395–8405.
[36] W. Zhao, C. Zhang, F. Geng, et al., ACS Nano 8 (2014) 10909–10919.
[37] Y. Jiang, T. Sun, X. Xie, et al., ChemSusChem 12 (2019) 1368–1373.
[38] J. Hou, Y. Wu, B. Zhang, et al., Adv. Funct. Mater. 29 (2019) 1808367.
[39] F. Du, L. Shi, Y. Zhang, et al., Appl. Catal. B: Environ. 253 (2019) 246–252.
[40] Z. Peng, D. Jia, A.M. Al-Enizi, et al., Adv. Energy Mater. 5 (2015) 1402031.
[41] S.Y. Pang, Y.T. Wong, S. Yuan, et al., J. Am. Chem. Soc. 141 (2019) 9610–9616.
[42] Z.W. Seh, K.D. Fredrickson, B. Anasori, et al., ACS Energy Lett. 1 (2016) 589–594.
[43] J. Liu, Z. Bao, Y. Cui, et al., Nat. Energy 4 (2019) 180–186.
[44] K. Yu, X. Pan, G. Zhang, et al., Adv. Energy Mater. 8 (2018) 1802369.
[45] Y. Wang, Y. Liu, Y. Liu, et al., J. Energy Chem. 54 (2021) 225–241.
[46] L. Yang, J. Guo, T. Yang, et al., J. Hazard. Mater. 402 (2021) 123741.
[47] J. Yu, W. Gu, H. Zhao, et al., Sci. China Mater. 64 (2021) 1723–1732.
[48] T. Yun, H. Kim, A. Iqbal, et al., Adv. Mater. 32 (2020) 1906769.
[49] X. Li, K. Ding, B. Gao, et al., Nano Energy 40 (2017) 655–662.
[50] W. Liu, N. Liu, Y. Yue, et al., Small 14 (2018) 1704149.
[51] Y. Ma, N. Liu, L. Li, et al., Nat. Commun. 8 (2017) 1207.